JOURNAL OF COMPUTATIONAL PHYSICS 76, 48–84 (1988)

Simulation of Rayleigh–Taylor Flows Using Vortex Blobs

ROBERT M. KERR*

L-321, Lawrence Livermore National Laboratory, P O. Box 808, Livermore, California 94550

Received November 7, 1986, revised May 15, 1987

An inviscid boundary-integral method is modified in order to study the single-scale Rayleigh–Taylor instability for arbitrary Atwood number. The primary modification uses vortex blobs to smooth the Green's function and suppress a finite time singularity in the curvature. Additional modifications to earlier codes such as using second-order central differences along the interface to accommodate spikes in the vorticity and spreading the nodes evenly along the interface to suppress clustering of nodes are designed to maintain resolution and accuracy To achieve second-order accuracy in time when the nodes are spread, an extra predictor step is needed that shifts the nodes before the variables are advanced The method successfully follows the development of a single mode to states with asymptotic velocities for the bubble and spike that depend on the Atwood number and are independent of the blob size Incipient droplet formation is observed

1. INTRODUCTION

While linear analysis of the Rayleigh–Taylor instability is well established and some modal and asymptotic analysis has been done, to study the full, large-amplitude nonlinear problem accurately one needs numerical methods that simulate fluids with highly convoluted interfaces. The original linear theory for the stability of an interface between two incompressible fluids of different density in a gravitational field is due to Lord Rayleigh [1], with Taylor [2] pointing out the relationship to accelerated fluid motion. Bellman and Pennington [3], Chandrasekhar [4], and Menikoff *et al.* [5] have extended the linear theory to include surface tension and viscosity. The initial value problem is discussed by Menikoff *et al.* [6] and Sharp [7] reviews the asymptotics and phenomenology at large amplitudes. Although, physically what initially disturbs the interface might be a shock (Richtmyer [8], Meshkov [9]), understanding the classical Rayleigh–Taylor problem is relevant because following the initial push from the shock the dynamics are incompressible to a good approximation. This is analogous to flow behind a shock front over an airfoil, which is also nearly incompressible. Numerically, incompressibility implies that elliptic interface tracking schemes are needed and the method outlined by Baker, Meiron, and Orszag [10] has reliably followed a single

* Permanent address: Geophysical Turbulence Program, National Center for Atmospheric Research, P O Box 3000, Boulder, CO 80307

0021-9991/88 $3 00

mode far into the nonlinear regime for some special cases. Eventually a numerical method that follows a multi-mode interface for arbitrary density ratios far into the non-linear regime, even to a turbulent scaling regime, would be desirable. But for now, good answers to well-posed problems are needed that can be used for inspiring and checking more powerful methods. It is not necessary that all aspects of the true physical problem be simulated. It is more important that a method converge in some sense to an asymptotic profile for a single initial mode, or at least converge to asymptotic values for the growth of the upper and lower extrema of the interface, known as the bubble and spike.

Most existing methods combine Eulerian and Lagrangian characteristics. The classic marker-in-cell work of Daly [11] uses an Eulerian grid and Lagrangian particles to mark fluids of different density. A physical viscosity is not used, but the mesh gives a numerical viscosity. In the method of Glimm *et al.* [12] the interface is on a quasi-Lagrangian mesh, that is, the nodes associated with the interface shift during the calculation. Both Daly and Glimm *et al.* show a spike of heavy fluid descending into the lighter fluid with vortices and rollup eventually forming on either side of the tip of the spike for finite density ratios.

Since all the grid methods are expensive and are limited in their ability to resolve a highly distorted interface, it would be desirable to have a relatively inexpensive, purely Lagrangian method that could represent a wide range of scales. This has been done reliably with boundary-integral methods in two limits of the Atwood number

$$A = \frac{\rho_1 - \rho_2}{\rho_1 + \rho_2},$$

where ρ_1, ρ_2 are the densities of the upper and lower fluids, respectively. In boundary-integral methods a surface is marked with Lagrangian particles that carry information, typically the vortex-sheet strength. Velocities and time derivatives of particle information are calculated from the surface information using the law of Biot-Savart and Green's functions. The limiting cases that have been studied are $A = 1$, when there is only a heavy fluid and a vacuum, and $A = 0$ in the Boussinesq approximation. In the Boussinesq approximation the gravitational field goes to infinity while the density ratio goes to 1, or the Atwood number goes to zero.

Baker, Meiron, and Orszag [10] solve the inviscid equations with a Lagrangian two-dimensional boundary-integral method that marks the interface with a potential-dipole sheet. Their method is equivalent to the vortex-sheet formulation of Baker, Meiron and Orszag [13] and Pullin [14], but has certain computational advantages. For $A = 1$, or one fluid, this method can resolve thin spikes that would be below the resolution of any grid method and has been used to study single and multimode perturbations for single-fluid and thin-shell geometries. Menikoff and Zemach [15] describe a boundary-integral method that uses conformal mapping to solve the potential equation for $A = 1$. Although identical initial conditions were not compared, comparisons of the curvature and acceleration at the tip of the spike indicate that the two methods agree closely. For $A = 1$ the most important

limitation of the boundary-integral methods is that iterations must be done. In the potential-dipole formulation an integro-differential equation involving the time-derivative of the dipole requires iteration. In the conformal mapping method a Newton–Raphson iteration is necessary.

Another case that can be treated by boundary-integral methods, but does not require an integro-differential equation, is Hele–Shaw flow. In this case the vortex strength is determined by an integral equation along the boundary and a viscosity-difference ratio replaces the Atwood number as the controlling parameter. The integral equation is designed to satisfy the viscous or pressure boundary conditions. The Kelvin–Helmholtz instability does not develop, but sharp curvature can develop and the integral equation must be solved by iteration. Node clustering along the interface can be a problem. Tryggvason and Aref [16, 17] have used a vortex-in-cell method to solve the Hele–Shaw problem and at late times observe elongated structures and in some cases droplet formation. Overman, Zabusky, and Ossakow [18] have solved a similar problem for ionized clouds in the ionosphere.

While inviscid methods work for $A = 1$, for $A < 1$ when two fluids are involved, Rayleigh–Taylor calculations using the method of [10] fail before displacements as large as the initial wavelength can develop. The reason is that while gravitational terms might initiate the Rayleigh–Taylor problem, shears develop quickly between two fluids and a singularity associated with the Kelvin–Helmholtz intability occurs in a finite time. This singularity could be considered the principal source of difficulty for two fluids in most of the methods mentioned. Our approach to the complete Rayleigh–Taylor problem will be to modify the boundary-integral scheme of [10] by smoothing the Green's function and suppressing this singularity. Because the Boussinesq case $A = 0$ avoids an integro-differential equation and manifests all the difficulties associated with the Kelvin–Helmholtz singularity, it will be treated first. Then the modifications to the integro-differential equation will be discussed.

II. Kelvin–Helmholtz and Boussinesq

It has been well demonstrated (Moore [19], Meiron, Baker, and Orszag [20], Krasny [21]) that when boundary-integral methods are applied to the Kelvin–Helmholtz instability that the vortex sheet develops a cusp, or a singularity in the derivative of the interface, in a finite time. In a real fluid the singularity does not occur and the interface rolls up because viscosity thickens the vortex sheet. Ho and Huerre [22] review the experimental evidence that the Kelvin–Helmholtz instability is characterized by a rolling up of the interface between the fluids. Large spectral calculations of the Kelvin–Helmholtz instability for constant density and a finite viscosity on two- and three-dimensional meshes discussed by Riley, Metcalf, and Orszag [23] have also shown the characteristic rollup. Grid methods designed for the inviscid case that do not fail must introduce some form of numerical viscosity to suppress the singularity and for a boundary-integral method to develop

beyond the cusp it must mimic the effect of viscosity and the vortex sheet must have a finite thickness.

The equation for the average velocity $\mathbf{U}(x, t)$ of two fluids along a vortex sheet is given by the law of Biot-Savart

$$\mathbf{U}(x, t) = \frac{1}{2\pi} P \int \frac{\mathbf{k} \times (\mathbf{x} - \mathbf{x}(e, t))}{|\mathbf{x} - \mathbf{x}(e, t)|^2} \gamma(e, t)\, de, \tag{1}$$

where

$$\gamma = \Gamma s_e \tag{2a}$$

is the local circulation in the arbitrary interface variable e, the vortex-sheet strength

$$\Gamma = (\mathbf{u}_1 - \mathbf{u}_2) \cdot \hat{s} \tag{2b}$$

is the jump in the tangential velocity across the interface, $\hat{s}$ is the unit tangent vector along the interface, $s_e^2 = z_e^* z_e$ is the derivative of the arclength when $z = x + iy$ is the complex position, and the subscript signifies the derivative with respect to e. For periodic boundary conditions in x, (1) reduces to

$$q^*(z) = \frac{1}{4\pi i} \int_0^{2\pi} \gamma(e) \cot \frac{1}{2} [z - z(e)]\, de + Q_E^*(z), \tag{3a}$$

where $q = u + iv$ is the complex velocity and Q_E is the external flow. The nodes along the interface can also follow a weighted average of the fluid velocities

$$\mathbf{q}^*(e) = q^*(e) + \frac{\alpha \gamma_e}{2 z_e}, \tag{3b}$$

where $|\alpha| \leqslant 1$ is the weighting factor.

Two approaches to smoothing the vorticity in boundary-integral formulations and making the simulations well-posed have been investigated. Pozrikidis and Higdon [24] have used contour dynamics similiar to Overman and Zabusky [25] to represent a sheet of finite thickness and constant vorticity. In their calculations the rollup is characterized by a thickening of the vortex sheet until a lump of vorticity is formed with thin streamers connecting it to the remnants of the vortex sheet. Shelley and Baker (private communication) have a similar calculation.

We will follow the approach of Krasny [26]. He thickens the vortex sheet by desingularizing or smoothing the Green's functions that are used to calculate velocities in the law of Biot-Savart. For example, the complex cotangent in (2), $\cot \frac{1}{2}[z(e) - z(e')]$, is replaced by the complex expression

$$\frac{\{\sin[x(e) - x(e')], -\sinh[y(e) - y(e')]\}}{\cosh[y(e) - y(e')] - \cos[x(e) - x(e')] + \delta^2}. \tag{4}$$

When the complete Rayleigh–Taylor problem is considered $\sec^2 \frac{1}{2}[z(e)-z(e')]$ will be replaced by

$$\frac{\{1-\cos[x(e)-x(e')]\cosh[y(e)-y(e')], \sin[x(e)-x(e')]\sinh[y(e)-y(e')]\}}{\{\cosh[y(e)-y(e')]-\cos[x(e)-x(e')]+\delta^2\}^2}. \tag{5}$$

This formulation is equivalent to multiplying the Green's function by a shape function as done by Beale and Majda [27]. That is, the vortices now represent vortex blobs whose size is given roughly by δ. The use of blobs of constant size is justified physically by considering that in an incompressible fluid there must be compression into the interface to balance the stretching along the interface as it rolls up. This compression will then balance the tendency for the viscosity in a physical fluid to spread the vorticity and a vortex sheet of finite thickness will be a good approximation. Using this formulation Krasny [26] sees the interface roll up into spirals that become tighter and whose outer rolls appear to reach asymptotic positions as $\delta \to 0$, suggesting that the large-scale dynamics are independent of δ as it goes to 0.

Inviscid linear theory, which applies to a vortex sheet with $\delta = 0$, is not correct after the Green's function is smoothed. This is expected if vortex blobs represent some of the effects of a true viscous calculation. Krasny finds that blobs modify the initial growth of the Kelvin–Helmholtz instability with a wavenumber dependence similiar to the linear theory of the effect of viscosity on the Rayleigh–Taylor instability [4]. In particular, the growth rate with vortex blobs is slower, especially for high wavenumbers.

The vortex-sheet formulation of the Boussinesq approximation to the Rayleigh–Taylor problem is identical to the formulation of the Kelvin–Helmholtz problem, except there is an added vorticity-production term. For $Ag \to constant$ as $A \to 0$ and the acceleration of gravity $g \to \infty$ the equation that will give the vortex growth is

$$\frac{\partial \gamma}{\partial t} - \frac{\alpha}{2}\frac{\partial}{\partial e}\frac{\gamma^2}{z_e z_e^*} = -2(Ag)\, y_e. \tag{6}$$

To solve the velocity equations (3a), (3b) and the vorticity production equation (6) numerically, the interface is discretized uniformly in e, which produces a one-dimensional mesh with non-uniform spacing in arclength. The variables stored at the nodes are their positions in x and y and the local circulation γ. A second-order Runge–Kutta algorithm is used for the time advancement because we find that second-order methods provide adequate convergence and accuracy without the difficulties of higher order methods. Second-order central differences are used to calculate the derivative of the position along the interface.

$$z_e^j = \frac{\partial z^j}{\partial e} = \frac{z^{j+1} - z^{j-1}}{2\,\Delta e}. \tag{7}$$

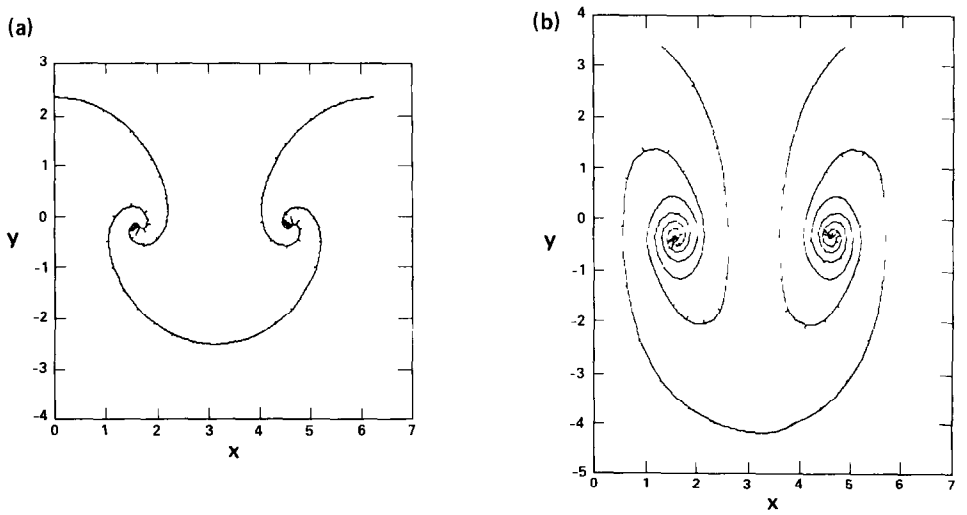

FIG. 1 Interface for the Boussinesq approximation and $\delta = 0.2$, 256 nodes, $Ag = 1$, $\alpha = 0$, and the length in the periodic direction is 2π The marks show every other node and are proportional to the vortex-sheet strength (a) $t = 5.5$, (b) $t = 7\,5$

It will be demonstrated that central differences are of second-order accuracy for these simulations.

Figures 1a, b show the interface at late times, $t = 5.5$, 7.5, for the Boussinesq limiting case using 256 nodes. The marks show every other node and are proportional to the vortex-sheet strength. It should be noted that in none of the interface profiles to be presented do the interfaces cross, although this representation of the vortex-sheet strength gives that appearance in some cases. The parameter that tells which interface the nodes should follow is $\alpha = 0$. The combined potential dipole-vortex method to be described was used. Identical results were obtained using a strictly vortex-blob method (1)–(6). For all our discussions of the basic numerical method, $\delta = 0.2$ will be used unless otherwise noted. The length in the periodic direction will be 2π and the integrals will be calculated using the trapezoid rule as in [10]. The initial conditions for the Boussinesq case are

$$x^j = \frac{2\pi}{n}(j-1) \tag{8a}$$

$$y^j = a\cos(x^j) \tag{8b}$$

$$\mu^j = 0.0001\cos(x^j) \tag{8c}$$

with $a = 0.1$. The local circulation

$$\gamma = \mu_e \tag{9a}$$

where

$$\mu = \Phi_1 - \Phi_2 \tag{9b}$$

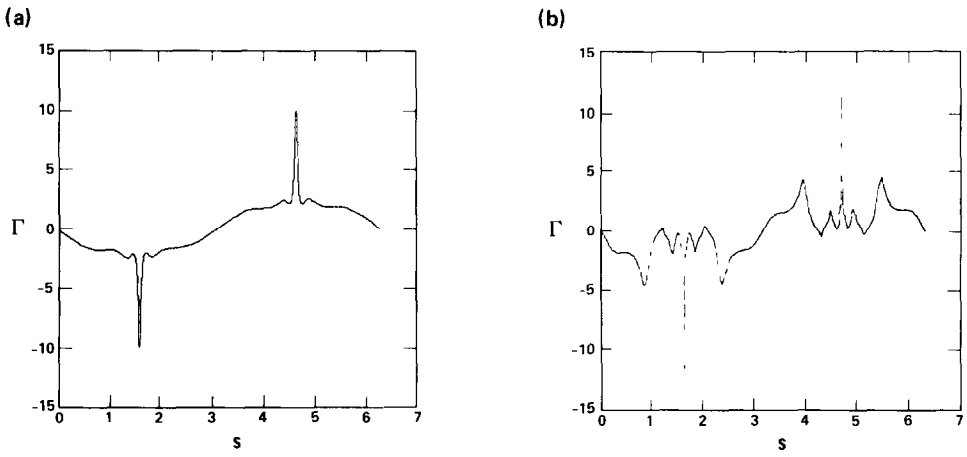

FIG 2 Vortex-sheet strength Γ vs arclength for the Boussinesq calculation and times of Fig 1

is the jump in the potential across the interface, or the potential dipole. μ is given a finite value so as to avoid floating-point errors in an analysis routine during the first timestep. The calculation was halted because what was wanted, a rollup, was well demonstrated. Figures 2a, b show the vortex-sheet strength Γ along the interface as a function of the arclength normalized to 2π. The primary peak is leading the rollup and the secondary peaks represent where vortex production has occurred on other turns.

Using the same approach, Tryggvason (private communication) has also calculated a rollup for the Boussinesq case. Using slightly different smoothings of the vortex sheet, two related problems have also been solved. Anderson [28] has solved the problem of a blob of slightly different density in a fluid and Lundgren [29] has solved for an axisymmetric axial flow.

Figure 3 shows the same calculation, but with $\delta = 0.05$ at $t = 4.25$. For smaller

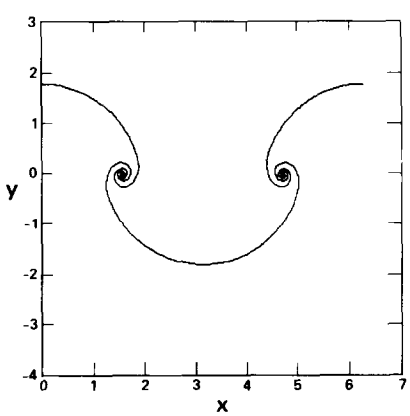

FIG 3. The same calculation as in Fig. 1, except $\delta = 0.05$, at $t = 4.25$

values of δ the calculation is closer to the inviscid case and while a cusp does not form, the rollup occurs earlier and is tighter. While this is consistent with the results of Krasny [26] for the Kelvin–Helmholtz problem, where the outer turns of the rollup appear to be approaching some limiting shape as $\delta \to 0$, in our calculation the interface does not appear to approach a limiting shape as rapidly, if at all. For example, the most obvious measure of large-scale growth, the height of the bubbles, does not converge in time. This is because the initial growth decreases as δ increases, a correction analogous to the effect of viscosity. This effect is greater for the Taylor problem than for the Kelvin–Helmholtz problem because the gravitational terms are always increasing the vortex strength.

While the profiles do not converge in time, there are other indications of convergence that are more important in the Taylor problem. For example, the final velocity for the single-mode problem is probably an important element of the rate-of-growth of the mixed region in a multimode problem. Figure 4 shows the bubble velocities versus time for the calculations in Figs. 1 and 3 with $\delta = 0.05$ and 0.2. For $\delta = 0.2$, an asymptotic velocity of about 0.8 is reached. For $\delta = 0.05$ the case is not as secure, but is indicated. This agrees with an asymptotic model using two vortices described by Aref and Tryggvason [30].

Aref and Tryggvason [30] have solved the Boussinesq case using a vortex-in-cell method. In this method the velocity is found by interpolating the vorticity from the interface onto a mesh and solving a Poisson equation instead of summing over Green's functions. Spreading the vorticity onto a mesh smooths the interactions, much as the vortex-blob method does. From crude comparisons, if $\delta = 0.2$ is the radius of blob and its diameter is 0.4, then for a periodic length of 2π, the equivalent vortex-in-cell calculation has $m = 16$ mesh spacings in the periodic direction.

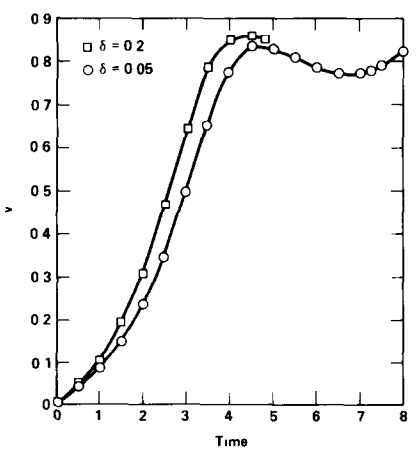

FIG 4 Bubble velocities vs time for the Boussinesq calculations in Fig 1, $\delta = 0\,2$, and Fig 3, $\delta = 0\,05$

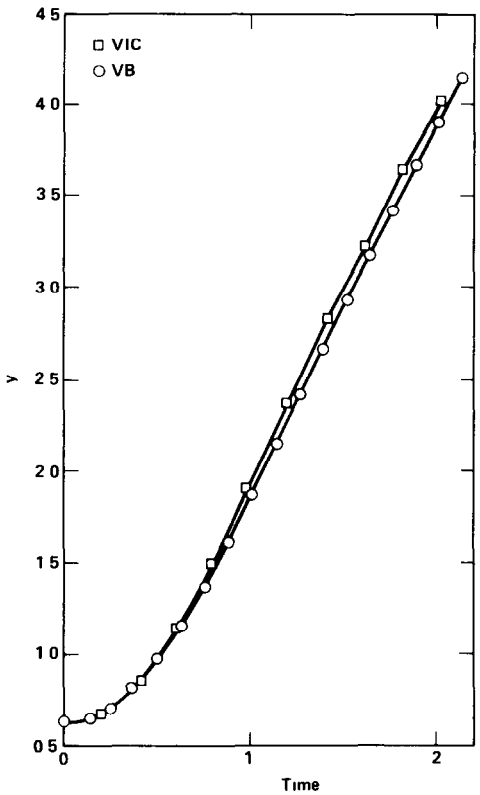

FIG 5 Growth of the bubble height for a Boussinesq calculation with the initial perturbation in (8b), $a = 0.2\pi$, and from [30] with $m = 16$

Figure 5 compares the growth of the bubble height for the two calculations. Profiles of the rollup and vorticity at the same times are almost identical. When properly normalized, the calculations in [30] give an asymptotic velocity of 0.8, in agreement with out calculations and the model in [30]. For an arbitrary Atwood number a similiar comparison based on mesh size might be done with the results of Daly [11]. His mesh was 20×60 and should have similiar viscous effects. Comparisons of higher Atwood number vortex blob calculations with a modification of the vortex-in-cell method are being done.

Baker, Meiron, and Orszag [10] formulate the vortex sheet using the potential dipole given by (9b). With periodic boundary conditions in x the potential can be found from the dipole by

$$\Phi(e) = \frac{1}{2\pi i} \int_0^{2\pi} \mu(e')\, z_e(e') \cot \frac{1}{2} [z(e) - z(e')]\, de' \tag{10}$$

and the average complex velocity at the interface is given by

$$q^*(e) = \Phi_e(e)/z_e(e). \tag{11a}$$

Without smoothing, this formulation for the velocity is equivalent to (3a) because the inviscid equations generate potential flow next to the interface. This can be seen by rewriting (11a) as

$$q^*(e) = \frac{1}{2\pi i} P \int_0^{2\pi} \mu(e')\, z_e(e') \left[\frac{x_e(e)\, \partial/\partial x + y_e(e)\, \partial/\partial y}{z_e(e)} \right] \cot \frac{1}{2} [z(e) - z(e')]\, de'. \tag{11b}$$

Next use the identity for $\delta = 0$,

$$\frac{x_e(e)\, \partial/\partial x + y_e(e)\, \partial/\partial y}{z_e(e)} \cot \frac{1}{2} [z(e) - z(e')] = \frac{\partial}{\partial z} \cot \frac{1}{2} [z(e) - z(e')]; \tag{12}$$

then replace $\partial/\partial z$ by $-\partial/\partial z'$, and finally use integration by parts to recover (3a). But for finite δ when (4) is substituted for the cotangent, this identity is not true and the two formulations for the velocity differ. By replacing $\partial/\partial x$ by $-\partial/\partial x'$ and $\partial/\partial y$ by $-\partial/\partial y'$ in (12) and using integration by parts the exact difference can be calculated

$$q^*(11) - q^*(3a)$$

$$= \frac{1}{2\pi i} P \int_0^{2\pi} \mu(e')\, \delta^2 \frac{(x_e - x_{e'}) \cos[x(e) - x(e')] + i(y_e - y_{e'}) \cosh[y(e) - y(e')]}{\{\cosh[y(e) - y(e')] - \cos[x(e) - x(e')] + \delta^2\}^2}\, de'. \tag{13}$$

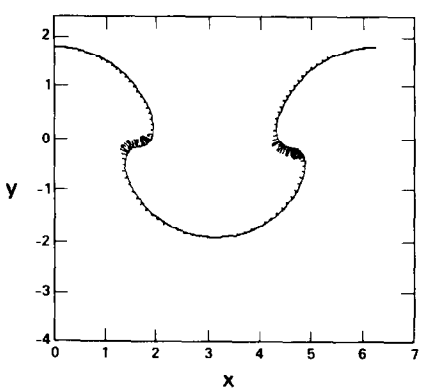

FIG 6 Interface using (10), (11) for the velocity in the Boussinesq approximation at $t = 4.8$ Initial conditions of (8a), (16a), (16b) used, 256 nodes, $Ag = 1$, $\delta = 0.2$, and $\alpha = 0$

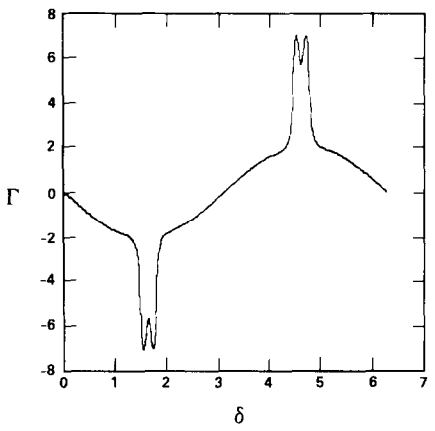

FIG 7 Vortex-sheet strength Γ vs arclength for the calculation in Fig. 6

The divergence of this will be non-zero, whereas using (3a) forces a divergence-free velocity field.

Figures 6 and 7 show the final well-behaved interface profile and vortex-sheet strength Γ in the Boussinesq approximation when (10), (11) are used instead of (3a) for the velocity. The double peaks in Fig. 7 are unphysical and can be explained by assuming that (10), (11) makes the rollup slightly slower and considering the effect of vorticity production. For the Kelvin–Helmholtz problem, which lacks vorticity production, the effect of using (10), (11) instead of (3a) is probably so small that the results might not be unphysical. However, in the Boussinesq case (6) adds vorticity to the outside of the rollup and any slowing of the rollup could prevent the formation of a single, well-defined, vorticity peak, such as in Figs. 2a, b. Calculations that use (10), (11) with a finite δ for $0 < A < 1$ also fail when double peaks like those in Fig. 7 develop. A vortex-blob method that smooths the Green's function for an arbitrary Atwood number, avoids these difficulties and retains the computational advantages of the potential-dipole method, while showing consistency with the Boussinesq case and $A = 1$, will be demonstrated.

III. Arbitrary Atwood Number

Following Baker, Meiron, and Orszag [10], for an arbitrary Atwood number the inviscid integro-differential equation for the time-derivative of the potential dipole is

$$\frac{\partial \mu}{\partial t} - \frac{\alpha \gamma^2}{2 z_e z_e^*} = -2A \left[\mathrm{Re}\left\{ \frac{\partial \Phi}{\partial t} \right\} - \frac{1}{2} q^* q - \frac{1}{2} \alpha \gamma \, \mathrm{Re}\left\{ \frac{q}{z_e} \right\} + \frac{\gamma^2}{8 z_e z_e^*} + g y \right], \quad (14a)$$

where the time derivative of the potential is

$$\frac{\partial \Phi}{\partial t}(e) = \frac{1}{4\pi i} P \int_0^{2\pi} \left[\frac{\partial \mu}{\partial t}(e') z_e(e') + \mu(e') \tilde{q}_e(e') \right] \cot \frac{1}{2} [z(e) - z(e')] \, de'$$

$$= -\frac{1}{8\pi i} P \int_0^{2\pi} \frac{\mu(e') z_e(e') [\tilde{q}(e) - \tilde{q}(e')]}{\sin^2(1/2)[z(e) - z(e')]} \, de'. \tag{14b}$$

[10] prefers this formulation over a vortex formulation because there are only first derivatives along the interface. The integro-differential equations required to determine the time-derivative of the vorticity are

$$\frac{\partial \gamma}{\partial t} - \frac{1}{2} \alpha \frac{\partial}{\partial e} \frac{\gamma^2}{z_e z_e^*} = -2A \left[\operatorname{Re} \left\{ \frac{\partial q^*}{\partial t} z_e \right\} - \frac{1}{2} \alpha \gamma \operatorname{Re} \left\{ \frac{q_e}{z_e} \right\} + \frac{1}{8} \frac{\partial}{\partial e} \frac{\gamma^2}{z_e z_e^*} + g y_e \right] \tag{15a}$$

and

$$\frac{\partial q^*(z)}{\partial t} = \frac{1}{4\pi i} \int_0^{2\pi} \frac{\partial \gamma(e)}{\partial t} \cot \frac{1}{2} [z - z(e)] \, de$$

$$- \frac{1}{8\pi i} P \int_0^{2\pi} \frac{\gamma(e) [\tilde{q}(z) - \tilde{q}(e)]}{\sin^2(1/2)[z - z(e)]} \, de. \tag{15b}$$

Calculations for an arbitrary Atwood number in either formulation proceed much as they do for the Boussinesq case, except for the need to solve integro-differential equations for the time derivatives of the potential dipole μ or local circulation γ. These equations are Fredholm equations of the second kind and can be solved by iteration. The iteration begins by using earlier timesteps to estimate the time-derivative. This is used on the right-hand side of (14b) or (15b) and a new time-derivative is calculated using (14a) or (15a), which then becomes a new estimate. The iteration proceeds until it is within a certain tolerance, or the number of iteration cycles exceeds a limit, in which case the calculation ends. Unless otherwise stated, we will refer to a calculation as ending when this occurs.

The potential-dipole formulation of the Rayleigh–Taylor problem in [10] is able to solve the single-mode problem for $A = 1$ far into the non-linear regime. Figure 8 shows a calculation that used 256 nodes along the interface at $t = 3$, 4, and 5.15, which is when the iteration of the Fredholm equation fails. The parameter that tells which interface the nodes follow in (3b), $\alpha = -1$, and gravity $g = 1$. Following [10] a cubic spline is used to calculate derivatives along the interface because in this case it can represent the sharp gradients better than central differences, which cause an identical calculation to fail at $t = 3.5$. [10] also used a higher order time advancement, but second-order Runge–Kutta gives satisfactory results and all the calculations to be discussed use that. The initial conditions are taken from a third-order expansion in ka for $A = 1$, where $k = 1$ is the wavenumber, and a is the

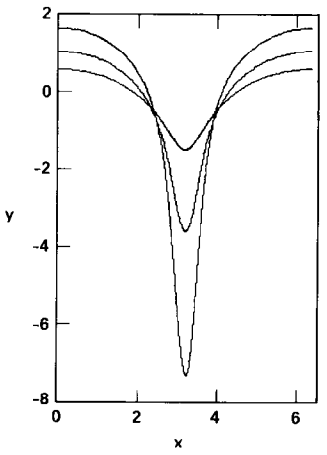

FIG 8 Interface for $A = 1$ and $\delta = 0$ at $t = 3$, 4, and 5 15 256 nodes used, $g = 1$, and $\alpha = -1$

amplitude of the initial disturbance. The position of the modes in x is given by (8a) and

$$y^j = a(1 + 0.5a^2)\cos(x^j) - 0.5a^2\cos(2x^j) - 0.75a^3\cos(3x^j) \tag{16a}$$

$$\mu^j = 2a(1 + 1.25a^2)\cos(x^j)\exp(-y^j) \tag{16b}$$

with $a = 0.05$. These initial conditions were used for all finite Atwood number calculations to be discussed. While this is clearly not correct for $A \neq 1$, where a different third-order expansion has been found, it does not affect the late-time behavior of the simulations to be discussed. Test calculations with the initial conditions of (8a)–(8c) have been investigated and the basics results, that is, the shape of the interface in the rollup region and the asymptotic velocities, were unchanged.

Figure 9 shows the vortex-sheet strength Γ as a function of normalized arclength

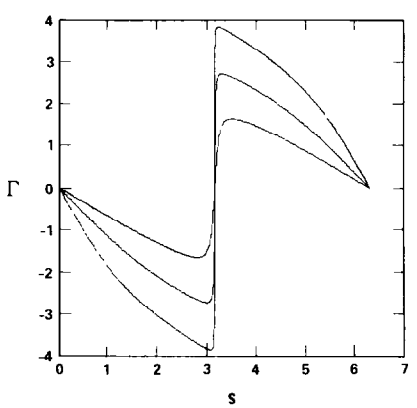

FIG 9 Vortex-sheet strength Γ vs arclength for the $A = 1$ calculation in Fig. 8 at $t = 3$, 4, and 5.1

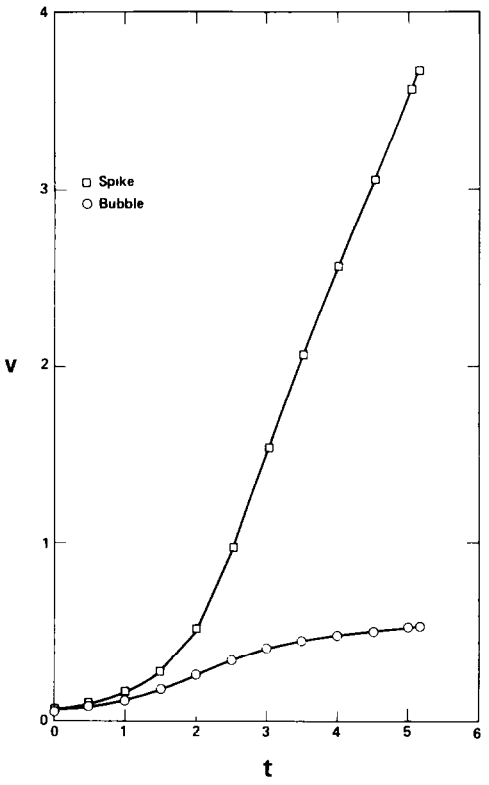

FIG 10 Bubble and spike velocities for the $A = 1$ calculation in Fig 8 vs time

at $t = 3$, 4, and 5.1. While the height of the vorticity jump at the tip of the spike grows with time, the shape of the vorticity profile does not change. Figure 10 shows the bubble and spike velocities as functions of time. The bubble reaches an asymptotic velocity while the spike is in free fall with the acceleration approaching 1, the gravitational constant g in (14a). Figure 11 plots the maximum absolute value of the curvature,

$$\frac{1}{R} = \frac{x_e y_{ee} - y_e x_{ee}}{(x_e^2 + y_e^2)^{3/2}} \tag{17}$$

as a function of time for this calculation, the calculation with $A = 0$ in Fig. 1, and the longest calculations for $A = 0.33$ and 0.8 to be discussed. The maximum curvature for $A = 1$ is at the tip of the spike and while it shows close to exponential growth, there are no indications that it will be singular in a finite time. However, because the curvature is increasing exponentially, the range of scales to be calculated must increase exponentially and the timestep must decrease exponentially. These constraints limit the ability of this simulation to continue beyond

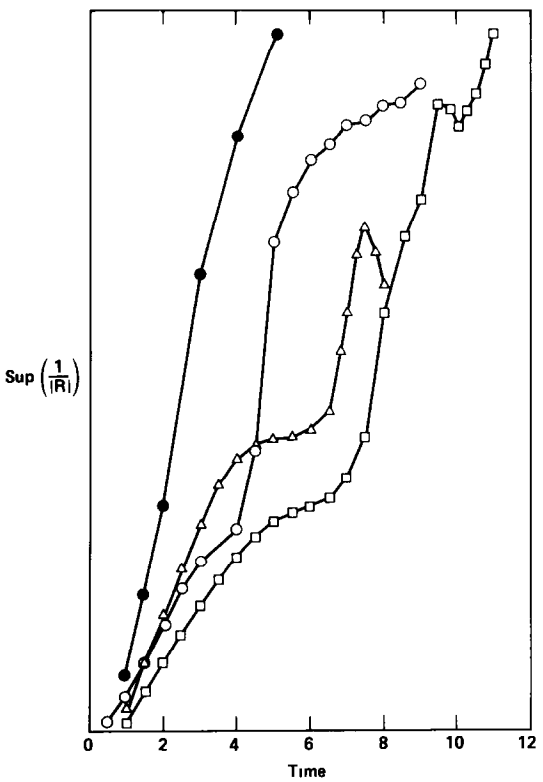

FIG 11 Maximum absolute value of the curvature (17) sup $|1/R|$ vs time ●, $A = 1$ calculation in Fig 8, ○, $A = 0$ calculation in Fig 1, □, $A = 0.33$ calculation in Fig 19, and △, $A = 0.8$ calculation in Fig 24

$t = 5.0$ which is when a calculation that used 64 nodes ended. The conformal mapping calculation of Menikoff and Zemach [15] and an earlier boundary-integral calculation by Baker, Meiron, and Orszag [13] obtain maximum amplitudes similar to those calculated here, but because our calculations start with smaller amplitudes, the curvature at the final time is greater.

While the method of [10] works remarkable well for $A = 1$, for $A < 1$ it fails rapidly. Figure 12 shows the interface and Fig. 13 the vortex-sheet strength Γ just before the Fredholm iteration breaks down for $A = 0.33$. These profiles were calculated using the method to be described with 64 nodes, $\alpha = -|A|^2$ and without node spreading. The Kelvin–Helmholtz cusp, which is indicative of the singularity in the derivative, is evident in Fig. 12. Therefore, the Green's function needs to be smoothed.

Smoothing (10), (11) to calculate the velocity for finite Atwood number leads to the same numerical problems as it did for the Boussinesq case. These can be avoided by using (3a) to calculate the velocities, with $\gamma = \mu_e$ (9a). Then (14a), (14b)

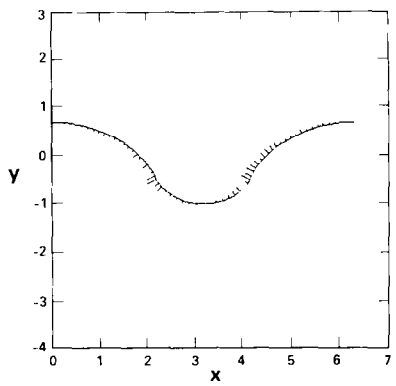

FIG 12 Interface for $A = 0.33$ and $\delta = 0$ at $t = 4.65$. 64 nodes used, $g = 1$, and $\alpha = -0.1089$

can be used to calculate the time-derivative of the potential dipole. Clearly, ordering the calculation of the Green's functions in (14a), (14b) differently might introduce a different smoothing and produce different results, just as occurred when (10), (11) were used instead of (3a). This has been investigated by using the pure vorticity formulation (15a), (15b) and the results were identical as long as the vorticity calculation lasted. The hybrid potential-dipole, vorticity method has been used because it resolves sharp structures better and converges longer than the pure vorticity method. Central differences (7) are used to calculate the interfacial derivatives.

Figure 14 shows a calculation for $A = 0.33$ with 128 nodes $\delta = 0.2$ and $\alpha = -|A|^2 = -0.1089$ at $t = 8.0$. Because α determines a weighted average of the fluid velocities at the interface through (3b), it indirectly determines how nodes are spread along the interface. Given adequate resolution, the results are independent of α and how the nodes are distributed. The major effect of changing α is that it will

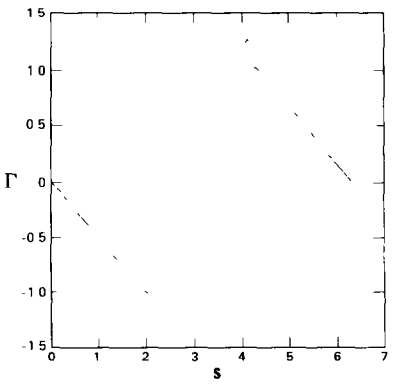

FIG 13 Vortex-sheet strength Γ vs arclength for $A = 0.33$ and $\delta = 0$ calculation in Fig 12.

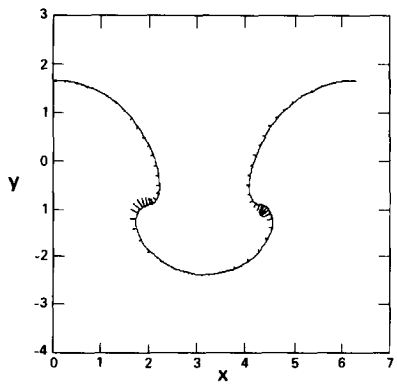

FIG 14 Interface for $A = 0.33$ and $\delta = 0\,2$ at $t = 8\,0$. 128 nodes used, $g = 1$, and $\alpha = -0\,1089$.

determine when too many nodes become clustered around a point, which causes the simulation to end due to instabilities near that point and inadequate resolution over the remainder of the interface. For all of the Atwood numbers to be discussed, if a node redistribution scheme is not used, choosing $\alpha = -|A|^2$ gave the best distribution of nodes along the interface and allowed the simulations to converge for the longest time. Given more control over the distribution of the nodes the simulations will converge longer, but to do this and maintain accuracy requires careful analysis of the time advancement.

IV. Spreading Nodes and Time Advancement

Our approach will be to spread the nodes by interpolating in arclength. The positions of the nodes in terms of arclength and the length of the interface can be determined by

$$s_{t+1} = s_t + \tfrac{1}{2}\,|z_e^{t+1} + z_e^t|\,\Delta e \tag{18}$$

with $s_0 = 0$ and $s_{n+1} =$ arclength. Parabolic, or Lagrange, interpolation is used to determine new values for the variables by the following steps. First, a parabola through the three nearest nodes for a variable μ_t is calculated as a function of the position s_t. That is, the coefficients a, b, and c in

$$\mu_{t-1} = c \cdot s_{t-1}^2 + b \cdot s_{t-1} + a \tag{19a}$$

$$\mu_t = c \cdot s_t^2 + b \cdot s_t + a \tag{19b}$$

$$\mu_{t+1} = c \cdot s_{t+1}^2 + b \cdot s_{t+1} + a \tag{19c}$$

are determined and the new value of μ_{new} at location s_{new} is

$$\mu_{\text{new}} = c \cdot s_{\text{new}}^2 + b \cdot s_{\text{new}} + a. \tag{20}$$

An algorithm for spreading the nodes based on a combination of radius of curvature and arclength in order to allow more resolution in regions of high curvature was investigated. However, hourglassing, a tendency for nodes to pair and for the distance between these pairs to go to zero, prevented its use. A better procedure that accomplishes the same objective is to run with the nodes evenly distributed until that fails, then go back to the last time saved and restart without node spreading and $\alpha = -|A^2|$ for low Atwood number. For higher Atwood numbers, $|\alpha| > 0.16$ should not be used. Comparisons with the calculation in Fig. 14, which does not use node spreading, show that using node spreading up to that time, $t = 8.0$, does not introduce any numerical smoothing that changes the physics of the simulation.

While spreading the nodes evenly along the interface prevents the numerical instability due to nodes clustering along the interface, it introduces new errors in the time advancement. For any multistep method, if spreading is done only at the end of the step, second-order errors in time are introduced by spreading the nodes. Several variations of second-order Runge–Kutta schemes that redistribute current and past times at each substep were experimented with and while some of these methods had much smaller errors than spreading only once per timestep, they were still first order. This is because the amount that spreading moves the nodes is of the order Δt and even if the nodes move very little, the error introduced by spreading cannot be less than Δt^2. This suggests that any higher order time-advancement scheme with spreading will inherently have second-order errors. The errors might

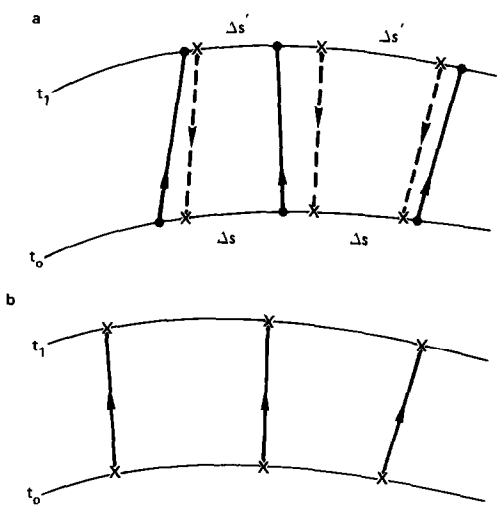

FIG 15. Substeps within each second-order Runge–Kutta timestep with node spreading. (a) A first-order Euler step advances the points from t_0 to t_1 (solid line) New positions for the nodes are chosen at t_1 such that their separation in arclength Δs is constant, shown by crosses at t_1 Based on those positions, the positions of the nodes at t_0 are spread, shown by dashed line and crosses at t_0 (b) Finally a standard second-order Runge–Kutta step is used to advance the nodes. The nodes are spread again at the end of the timestep

be small initially, but once the Kelvin–Helmholtz rollup begins, these errors can be expected to dominate the calculation. Zabusky and Overman [31] have spread the points in their simulation less frequently than in our calculations, but have not checked accuracy. Their spreading must introduce second-order errors, but it would be interesting to see if doing it less frequently decreases or increases the error. Since their problem is not as singular as the full Rayleigh–Taylor case, it might not be as important. Another approach that might avoid node redistribution would be to follow Pullin [14] and choose α as a function of arclength.

The trick to making the time advancement second-order is to shift the nodes at the beginning of the timestep based on where they will be at the end of the timestep. This is analogous to the semi-Langrangian schemes used in some meteoroligical applications [32]. A first-order Euler step advances the points. New positions for the nodes are chosen and based on those positions, the positions of the nodes at the beginning of the timestep are spread. Then a standard second-order Runge–Kutta step is used to advance the nodes. The nodes are spread again at the end of the timestep. A second-order predictor for the new locations was investigated, but there was no improvement. Figure 15 demonstrates the step. To demonstrate how successfully the method gives second-order accuracy, Fig. 16 compares several simulations with $A=0.33$, $\delta=0.2$, $n=64$, and $g=1$ for different, constant timesteps, indicated by the superscript j, as a function of time using second-order Richardson extrapolation

$$\sup(R1)=\frac{\sup|z_i^{(j)}-z_i^{(0)}|}{CFL^{(j)^2}-CFL^{(0)^2}}. \tag{21}$$

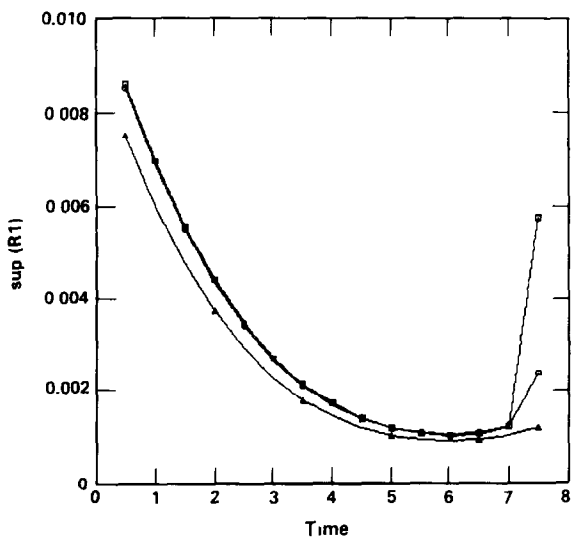

FIG 16 Second-order Richardson extrapolation sup($R1$) (21) as a function of time for several

Richardson extrapolation usually uses the timestep Δt, but it is more convenient in this case to compare the errors using the effective Courant number defined below (22). Satisfactory second-order convergence is seen for $\Delta t = 0.005$ to 0.5. Even using Δt as large as 0.5 with 64 nodes, as late as $t = 8.0$ there were not any obvious differences between the interface calculated and that shown in Fig. 14.

Figure 16 does not show any departures from second-order accuracy that would suggest a Courant-like condition. That is, for larger values of Δt the accuracy does not depart from second-order at earlier times. Instead, as the calculation enters the rollup region and loses resolution, smaller timesteps lose second-order accuracy first. Despite this trend, the Fredholm iteration cycle does break down at earlier times for larger values of Δt and the following Courant-like condition is suggested

$$\Delta t = CFL \cdot \min \frac{|z_e(i)|\, \Delta e}{|q|} \left(1 - \frac{|z_e(i+1) - z_e(i)|}{|z_e|}\right). \tag{22}$$

The first factor in (22) is similar to the common Courant condition based on the velocities and spacing between points (18). The second part is a correction based on the radius of curvature. Since a proof for a Courant condition on a Lagrangian interface is not known, this condition is entirely empirical. Because Fig. 16 shows that second-order accuracy is lost as roll-up begins at $t = 7.0$, the node spreading algorithm has not been used very far into the roll-up region in the calculations to be discussed. Whether node spreading is used or not, in most of the calculations to be discussed $CFL = 0.25$.

The Fredholm equation for the time-derivative of the potential dipole in (14a), (14b) is solved by Jacobi iteration; that is, the values of $\partial\mu/\partial t$ on the right-hand side of (14b) do not change during an iteration step. Second-order interpolation based on past time derivatives was used for the initial estimate because experience shows that the number of iteration cycles tends to be lowest when the order of interpolation of the initial estimate is the same order as the time advancement. Past time derivatives of the dipole are interpolated along with the current values of the position and dipole when the nodes are spread. Overman, Zabusky, and Ossakow [18] have found that the number of iteration cycles can be reduced by using Gauss–Seidel instead of Jacobi iteration in solving their integral equation. In Gauss–Seidel the values of $\partial\mu/\partial t$ on the right-hand side are updated while new values are found. Due to the sensitivity of the integro-differential equation in our problem, Jacobi iteration has been chosen because the approach to convergence is symmetric. Overman (private communication) has verified that Jacobi iteration is better than Gauss–Seidel for the Rayleigh–Taylor problem.

Using these methods helped increase the timestep, decrease the number of iteration cycles, and reduce the computation time, which increases as n^3, with n^2 for the quadrature and an extra n for reducing the timestep. The longest simulations with 256 nodes required 2.6 h on the 7600 and had to be rewritten to put only what was necessary in small-core memory. With further minor changes up to 512 points

could be simulated, but this would be prohibitive unless a method for reducing the cost of the quadrature is found. This will be discussed in the conclusion.

V. High-Wavenumber Filtering and Spatial Convergence

While timestep refinement has been shown to give temporal convergence, simply adding nodes does not always give spatial convergence. Since the linearized growth rates of the Rayleigh–Taylor and Kelvin–Helmholtz instabilities increase with wavenumber, high-wavenumber noise due to numerical error or machine round-off errors can grow faster than high-wavenumber components would evolve in an ideal calculation. Most earlier calculations have started with very large initial perturbations so that the growth of the dominant mode stretches the interface and most of high-wavenumber noise is damped. But to start with small perturbations, a large number of nodes, and eliminate this type of numerical intability it is necessary to selectively apply high-wavenumber filters as suggested by Krasny [21]. He has shown that by using filtering that calculations with low floating-point precision can reproduce unfiltered calculations that use greater floating-point precision.

The objective is to set the error-induced coefficients for high wavenumbers to zero at early times, but turn off the filter at a given wavenumber once the interface has evolved into that wavenumber. This can be done by Fourier transforming the positions and strengths and analyzing the amplitudes of the modes as the wavenumber increases. If two successive coefficients are below a value (10^{-7} is used on the 7600), then the coefficients for these and for all higher wavenumbers are set to zero. The first wavenumber set to zero is saved and on the next timestep the analysis is repeated, beginning at this wavenumber. This approach removes the need to do the order of n tests for each variable each timestep. The filtering is not needed for calculations with 64 nodes and does not change the results when applied. When the filtering is used with 128 or more nodes the calculations reproduce the results for 64 nodes and continue the calculation further. We have found that when a perturbation is sufficiently large, either due to initial conditions or evolution from a small initial perturbation, that the filter is not necessary and it is turned off. [13, 14] avoid using a high-wavenumber filter on the initial conditions by initializing with a sufficiently large perturbation.

While cubic splines work best for $A = 1$, for $0 \leqslant A < 1$ central differences (7) are better. The reason might be that the vortex-sheet strength Γ had only a discontinuity for $A = 1$, whereas for $A < 1$, as in Fig. 2, Γ has a spike, which behaves as a δ-function and is more singular. The need to handle this is especially critical for $0 < A < 1$ when the derivatives in (14a), (14b) must be calculated. Another way to look at this is that the potential dipole μ has a discontinuity in only its first derivative for $A = 1$ and for $A = 0$, μ is discontinuous. Although central differences are only first order if the mesh is not uniform and the nodes in this simulation are not spaced uniformly in arclength, because the nodes are spaced uniformly in the variable e central differences are second order in these simulations. Figure 17 com-

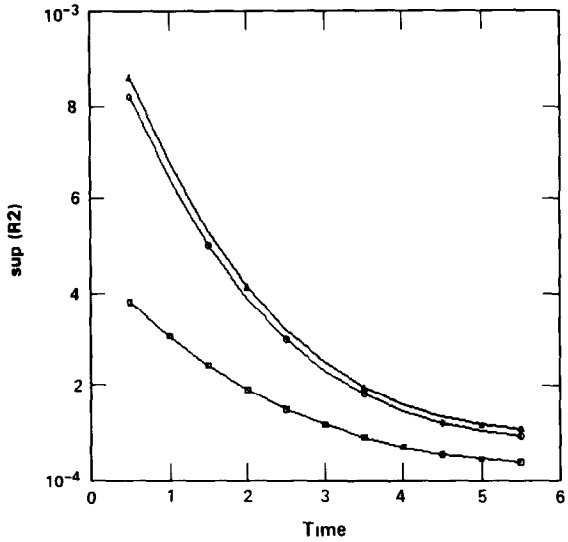

FIG 17 Second-order Richardson extrapolation sup($R2$) (23) as a function of time for several simulations with different meshes and $A = 0.33$, $\delta = 0.2$, and $g = 1$ $n_0 = 256$, $\Delta t_0 = 0.005$ in (26) □, $n = 32$, $\Delta t = 0.5$; ○, $n = 64$, $\Delta t = 0.25$, △, $n = 128$, $\Delta t = 0.125$

pares the errors on different meshes for the same effective Courant number using second-order Richardson extrapolation

$$\sup(R2) = \frac{\sup |z_i^{(J)} - z_i^{(0)}|}{(n_0/n^{(J)})^2\, CFL^{(J)^2} - CFL^{(0)^2}}. \tag{23}$$

By repeating these calculations without node spreading, all of this error can be attributed directly to using central differences, and not node spreading.

Despite sacrificing higher order spatial accuracy, for finite Atwood number, even–odd numerical errors eventually develop around the vortex peak at late stages. This could be due to the inability to provide adequate node distribution around both the vortex peak and a new cusp that forms along the interface. Additional smoothing techniques that can be used to extend the calculations further are discussed in Kerr [33].

VI. RESULTS

The analysis will start at a low Atwood number, $A = 0.1$, then look at increasing Atwood numbers to show consistent behavior from $A = 0$ to $A = 1$. $A = 0.33$ and $A = 0.8$ will be considered most carefully. For all the cases to be presented, the initial conditions of (8a), (16a), and (16b) are used. As noted, test calculations using the initial conditions of (8a)–(8c) do not show any significant differences.

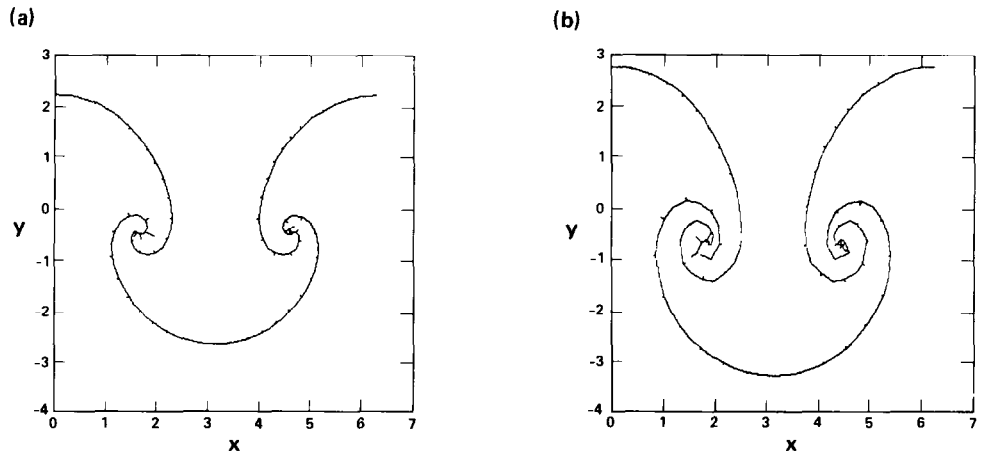

FIG 18 Interface for $A = 0.1$, 128 nodes used and $g = 5$ Node spreading used until $t = 6.5$, when the nodes were allowed to move with $\alpha = -0.01$· (a) $t = 6.5$, (b) $t = 8.5$

Figures 18a, b show the interface profile for $t = 6.5$, 8.5 for $A = 0.1$, which is close to the Boussinesq case. The vortex-sheet strength Γ along the interface for $t = 7.5$, 8.5 is shown in Fig. 19a, b. The gravitational constant in (14a), $g = 5$, $\delta = 0.2$, and 128 nodes were used. The calculation used node spreading until $t = 6.5$, when the nodes were allowed to move with $\alpha = -0.01$. A rollup similiar to the Boussinesq case occurs, but with a small droplet at the end of the rollup. The vorticity distribution initially forms two peaks associated with the two rollups, much like the Boussinesq case, but near the end of the calculation the sides of these peaks towards the bubble cannot be resolved. At the final time secondary peaks similiar to those in the Boussinesq case appear.

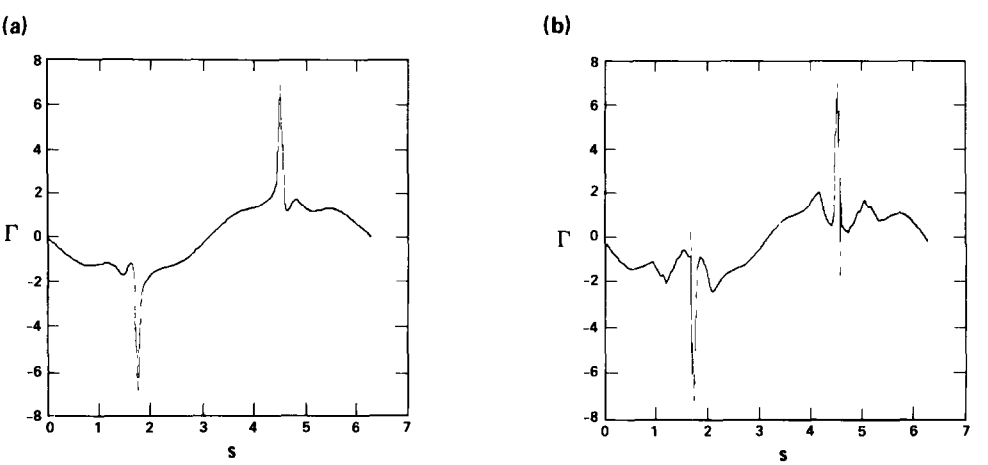

FIG. 19 Vortex-sheet strength Γ vs arclength for the $A = 0.1$ calculation in Fig 18 (a) $t = 7.5$, (b) $t = 8.5$.

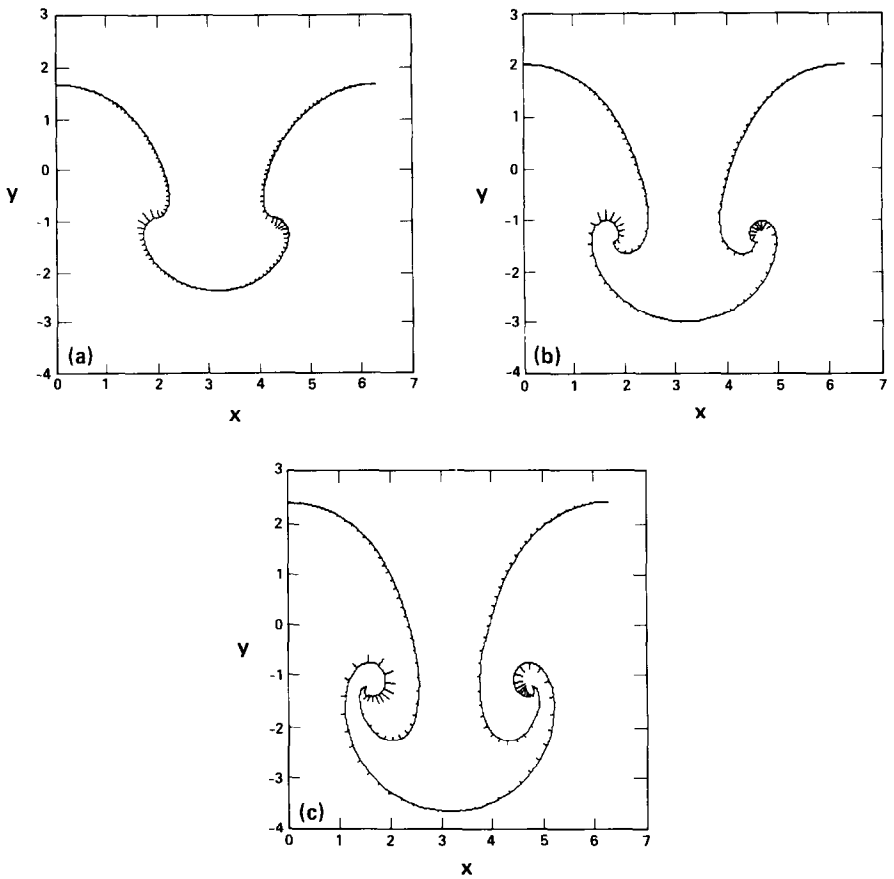

FIG 20 Interface for $A = 0.33$; 256 nodes used and $g = 1$. Node spreading used until $t = 8$, when the nodes were allowed to move with $\alpha = -0.1089$. (a) $t = 8$, (b) $t = 9$, (c) $t = 10$

Figures 20a–c and 21a–c show the interface and vortex-sheet strength Γ for $A = 0.33$ and $t = 8$, 9, and 10. 256 nodes were used, $\delta = 0.2$, gravity $g = 1$; node spreading was used until $t = 8.0$; then the nodes moved with $\alpha = -0.1089$.

Figure 20a shows an early stage of the rollup at $t = 8.0$ that is characterized by a broadened spike. By $t = 9.0$ the rollup is well developed, but unlike $A = 0.1$ where there is considerable rollup before a droplet at the end of the rollup is obvious, here the droplet forms immediately and a spiral rollup is only beginning at $t = 10$. Once it is formed, the size of the droplet leading the rollup appears to be constant and the vorticity profiles evolve much like they did for $A = 0.1$. Single vortex peaks develop in the early stages of the rollup, as in Fig. 21a, but a major difference at later times between Fig. 21c for $A = 0.33$ and Fig. 19b for $A = 0.1$ is that secondary vorticity peaks towards the spike are suppressed in Fig. 21c and there is a large,

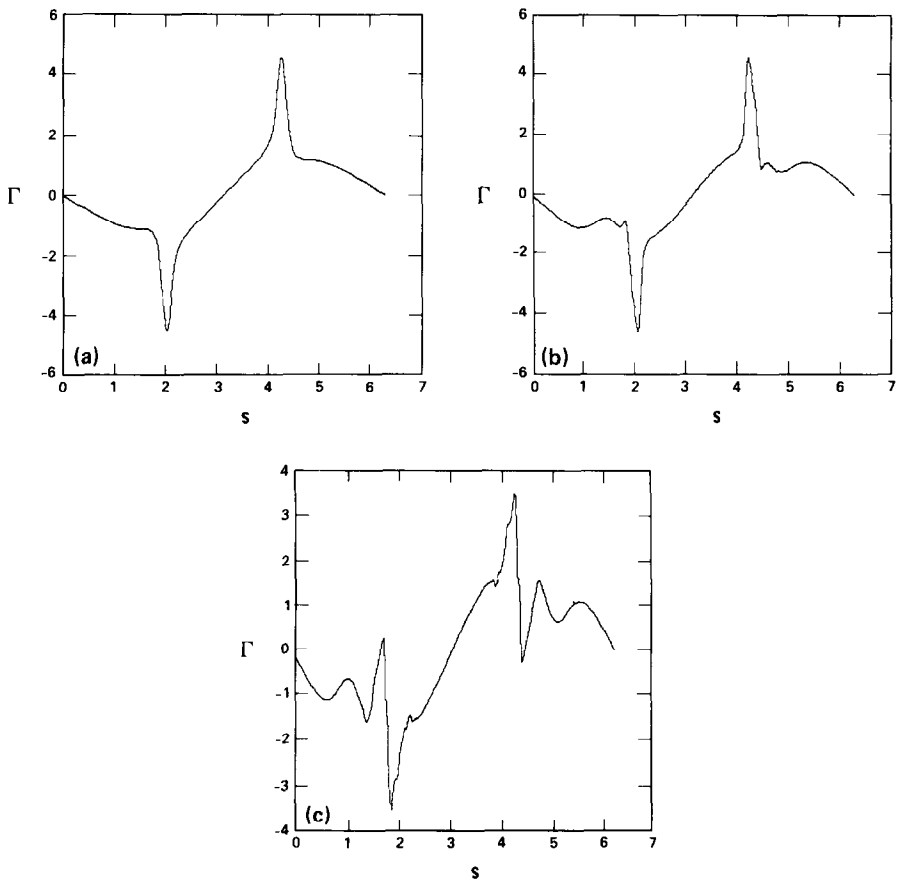

FIG 21 Vortex-sheet strength Γ vs arclength for the same times as the $A = 0.33$ calculation in Fig 20

relatively constant vorticity gradient that foreshadows behavior at $A = 1$ as in Fig. 10.

Figure 22 shows the final well-behaved profile at $t = 7.5$ for $A = 0.33$ and the same conditions as in Figs. 20 and 21, except $\delta = 0.1$. With smaller δ the rollup occurs earlier and is tighter, but when scaled the outline of the rollup is similiar to that in Fig. 20c at $t = 10$. Figure 23 shows the bubble and spike velocities as functions of time for $\delta = 0.0$, 0.1, and 0.2. The finite-delta velocities converge with time as they did for $A = 0$.

Following [10] the potential energy can be calculated from the interface shape by

$$\frac{4E_P}{\rho_1 + \rho_2} = 2Ag \int_0^{2\pi} y^2 x_e \, de \tag{24}$$

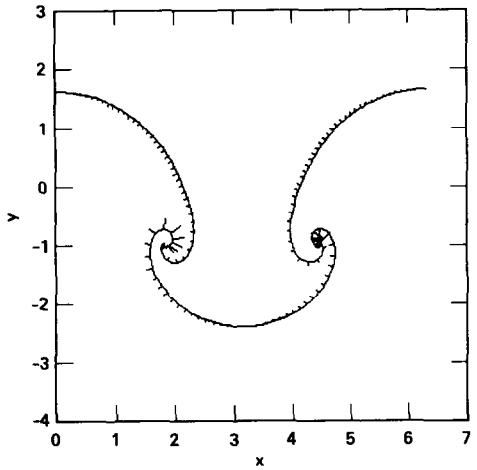

FIG 22 Interface for $A = 0\,33$ and $\delta = 0\,1$ at $t = 7\,5$ with the remaining conditions identical to the calculation in Fig 20

and the kinetic energy can be calculated by

$$E_K = \frac{1}{2}\rho_2 \int_{R_2} (u^2 + v^2)\, dA + \frac{1}{2}\rho_1 \int_{R_1} (u^2 + v^2)\, dA. \tag{25}$$

When $\delta = 0$ the kinetic energy is determined by

$$\frac{4E_K}{\rho_1 + \rho_2} = \int_0^{2\pi} \psi\gamma\, de + 2A \int_0^{2\pi} \psi\phi_e\, de, \tag{26}$$

where ψ is the stream function. Deriving (26) from (25) requires potential flow away from the interface, which does not occur when $\delta \neq 0$. Despite this, calculating (26) as an approximation to the kinetic energy and comparing it with the potential

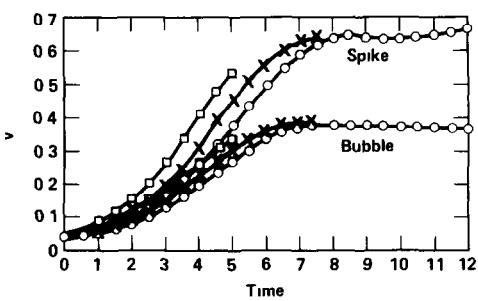

FIG. 23 Bubble and spike velocities vs time for the $A = 0\,33$ calculations in Fig. 20, $\delta = 0\,2$, Fig 23, $\delta = 0\,1$, and Fig. 12, $\delta = 0$

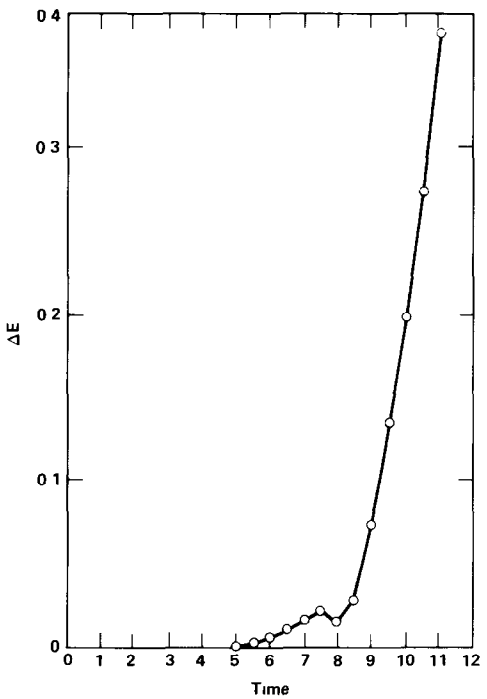

FIG 24 Effective dissipation of energy $PE - KE - (PE - KE)_0$ vs time

energy gives some indication of how much dissipation occurs during the rollup. Keeping track of both the potential and kinetic energies during the simulations also provides a useful tool for checking whether a simulation is behaving correctly and tracing errors. Figure 24 plots $PE - KE - (PE - KE)_0$. The dissipation of energy induced by the rollup is evident after $t = 8.0$.

Figures 25a–c and 26a–c show the interface and vortex-sheet strength Γ for $A = 0.8$, 256 nodes, $g = 1$, and $\delta = 0.2$ at $t = 5$, 7, and 8 and Fig. 27 shows the bubble and spike velocities. Node spreading was used until $t = 7.11$, then nodes moved with $\alpha = -0.16$. At $t = 5$ the calculation looks like the earlier stages of $A = 1$, except that the end of the spike is a bit wider and the back sides of the vorticity peaks are different. The vorticity profile is similiar to the vorticity profile for $A = 0.33$ and $\delta = 0$ in Fig. 13. At $t = 7$ in Fig. 25b a droplet is clearly trying to break off. This very "viscous" (large δ) calculation is similar to pictures of droplet formation in the Hele–Shaw case of Tryggvason and Aref [16, 17], where shear and rollup do not occur. Daly [34] gets droplet formation for this order of an Atwood number with surface tension. Both surface tension and viscosity dissipate energy and if dissipation is important in droplet formation, then both mechanisms should cause droplet formation. At $t = 8$ in Fig. 25c the rollup is similar to the initial stages for $A = 0.33$, but the side droplets are larger and the head of a spike is not as wide as in

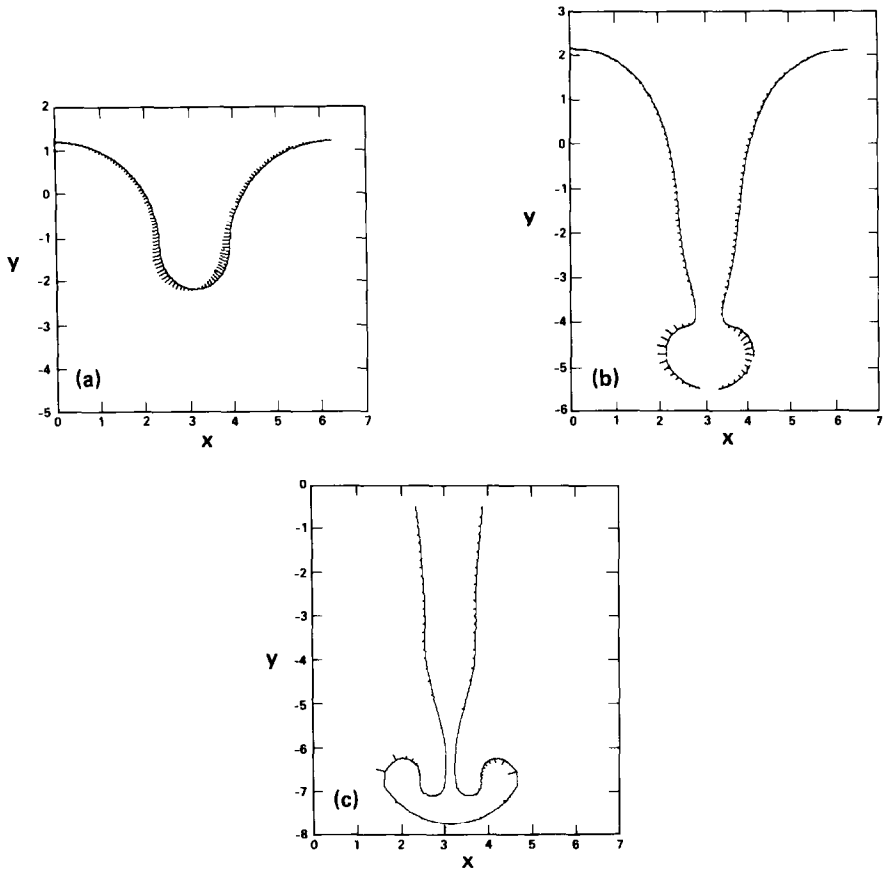

FIG 25 Interface for $A = 0.8$, 256 nodes used and $g = 1$. Node spreading used until $t = 7.11$, when the nodes were allowed to move with $\alpha = -0.16$· (a) $t = 5$, (b) $t = 7$, and (c) $t = 8$

Fig. 20b. A second bulge is forming in the middle of the spike as the rolled-up tip of the spike is separating.

For $A = 1$ the asymptotic state is probably characterized by a spike in free-fall and a bubble with an asymptotic velocity. For all $A < 1$ studied, asymptotic velocities for both the spike and the bubble are eventually indicated. For $A = 0$ the bubble and spike have the same final velocity. Figure 28 shows the asymptotic velocities normalized by the Atwood number, strength of gravity, and wavenumber

$$\tilde{v} = \frac{v}{(Ag/k)^{1/2}} \tag{27}$$

for a range of Atwood numbers. Two calculations with 128 nodes, $A = 0.5$ and 0.65, and $\delta = 0.2$ were done to fill out this curve. Values for negative Atwood numbers

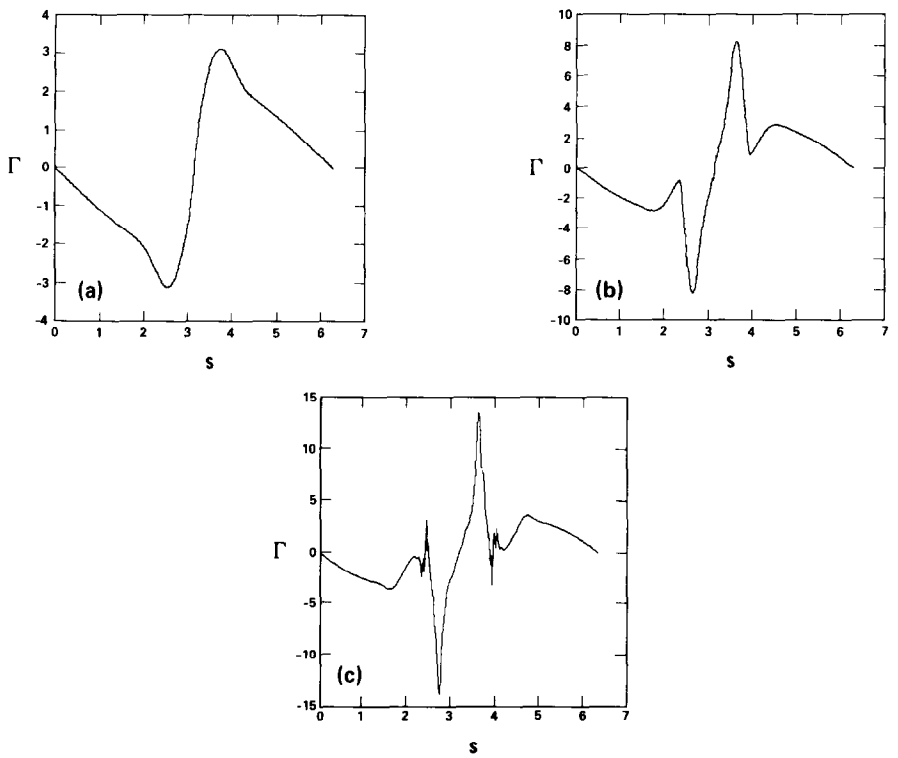

FIG 26 Vortex-sheet strength Γ vs arclength for the same times as the $A = 0.8$ calculation in Fig. 25

are the spike velocities. The bubble velocity for $A = 1.0$ is well determined from earlier calculations and it is encouraging that our calculations seem to approach this value as the Atwood number increases. The spike velocity increases rapidly as $A \to 1$, as it should since at $A = 1$ it is in free-fall. Reproducing these velocities could serve as a test for future methods.

For $A < 1$ and $\delta = 0$, the Kelvin–Helmholtz singularity that occurs in a finite time is characterised by a singularity in the curvature. In order to understand the limitations of simulations with a finite δ better Figs. 29a–h show the curvature profiles (17) for several times for the simulations discussed for $A = 0.0$, 0.33, and 0.8 with $\delta = 0.2$ and $A = 1$ with $\delta = 0$. The maxima of the curvature profiles were plotted in Fig. 11. For all Atwood numbers there is initially an exponential growth in the curvature at the tip of the spike, but for $A < 1$ Fig. 11 shows that this growth decreases. Figures 29a, c for $A = 0$ and 0.33 show that this is due first to a flattening of the curvature profile, then to an inversion. The edges of this inversion represent the rollup region and eventually a double spike appears, as in Fig. 29b for $A = 0$, which indicates that a cusp has formed in the interface. As the cusp develops the maximum curvature in Fig. 11 for $A = 0$, 0.33, and 0.8 increases again. For $A = 0$

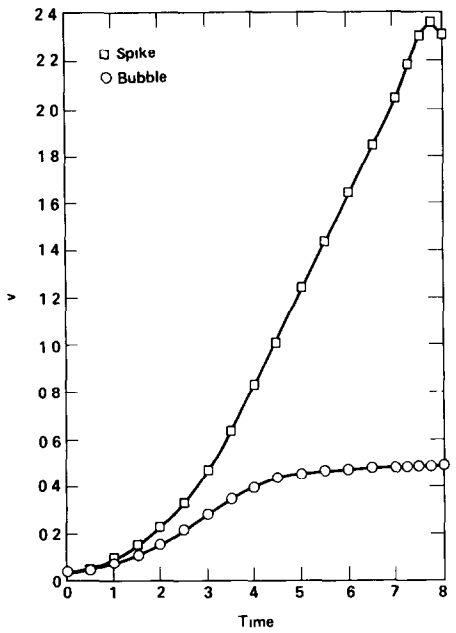

FIG 27 Bubble and spike velocities vs time for the $A = 0.8$ calculation in Fig 25

this cusp is coincident with the peak of the vorticity, which implies that by allowing the nodes to follow the average velocity of the fluids and naturally accumulate at this point both the curvature and vorticity can be adequately resolved and the simulation can continue to late times. There are no indications that the curvature is infinite in a finite time as occurs when $\delta = 0$. Secondary peaks in the curvature move away from the leading cusp much as occurs with the vorticity peaks in Figs. 2a, b. For $0 < A < 1$ the secondary peaks appear, as in Fig. 29d for $A = 0.33$, but are not symmetric about the cusp. In addition, for $0 < A < 1$ the cusp is not

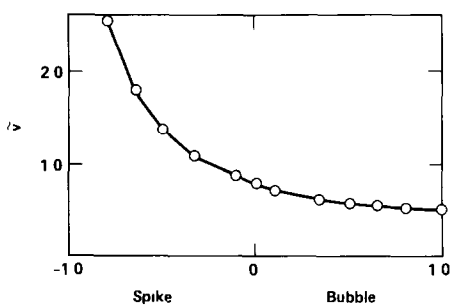

FIG 28 Asymptotic velocities normalized by (33) vs Atwood number Values for negative Atwood number are the spike velocities

coincident with the vorticity peak, which can be seen by carefully comparing Figs. 29d and 21b for $A = 0.33$. This implies that it is impossible to allow the nodes to naturally concentrate around a single location within a rollup and adequately resolve both the cusp and the vorticity peak and is a source of the final difficulties encountered in simulating all Atwood numbers. It could also be related to droplet formation and why the rollup is generally more complicated than for $A = 0$. There

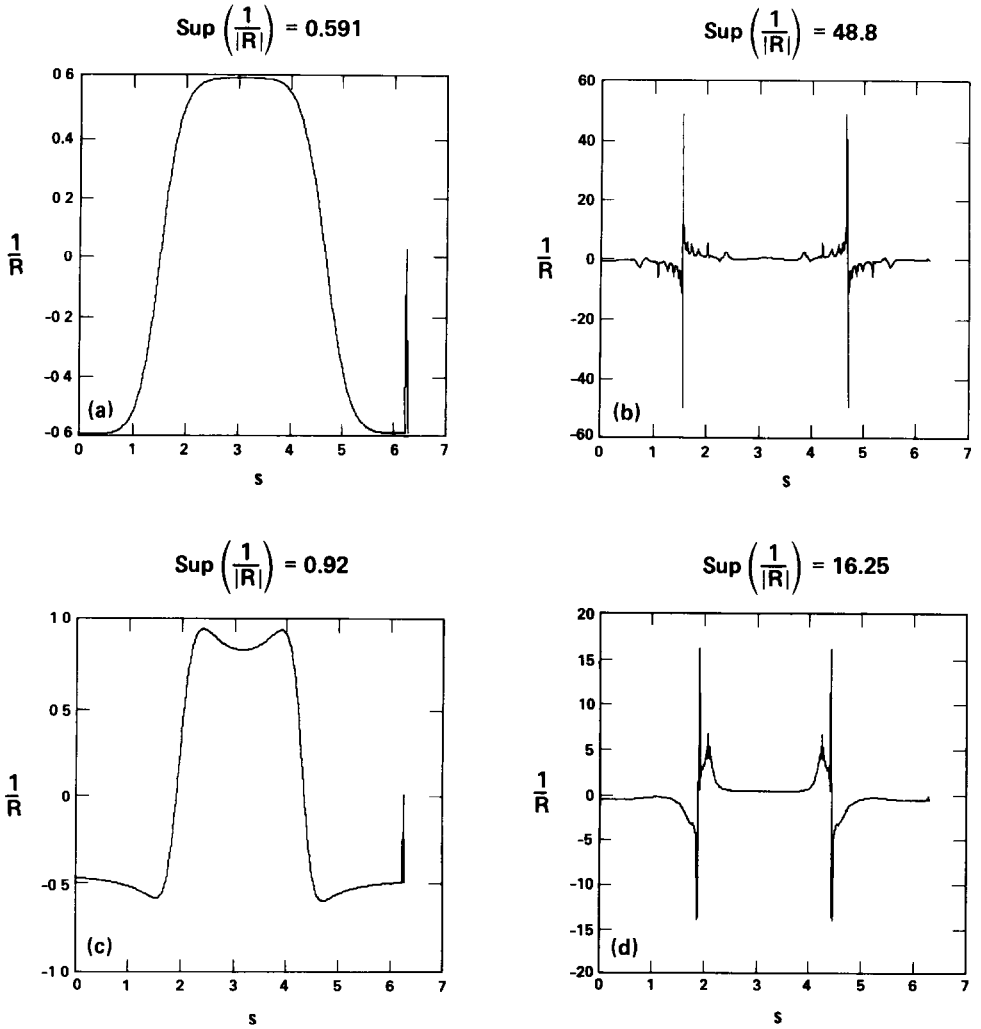

FIG 29 Inverse curvature profiles (17) $1/R$ vs arclength (a, b) From Boussinesq, $\delta = 0.2$ calculation in Fig 1 at $t = 3.5$ and 8.0, sup $|1/R| = 0.59$, 48, (c, d) From $A = 0.33$, $\delta = 0.2$ calculation in Fig. 20 at $t = 6.5$ and 9.0, sup $|1/R| = 0.92$, 16, (e, f) From $A = 0.8$, $\delta = 0.2$ calculation in Fig 25 at $t = 5.5$ and 6.5, sup $|1/R| = 1.7$, 2.1, (g, h) From $A = 1$, $\delta = 0$ calculation in Fig 8 at $t = 2$ and 4, sup $|1/R| = 0.89$, 31.

are similiarities between this behavior and other two-dimensional calcutions where a secondary cusp is driven by concentrations of vorticity. In a vortex-sheet calculation by Krasny [35] the concentrations are characterized by tight spirals. In a large spectral simulation of the two-dimensional Navier–Stokes equations with Taylor–Green initial conditions by Brachet, Meneguzzi, and Sulem [36] the cusps appear to be associated with the appearance of a k^{-3} entropy spectrum.

For $A = 1$ the curvature develops only a single peak at the tip of the spike and never has the cusp or double peak associated with the Kelvin–Helmholtz instability.

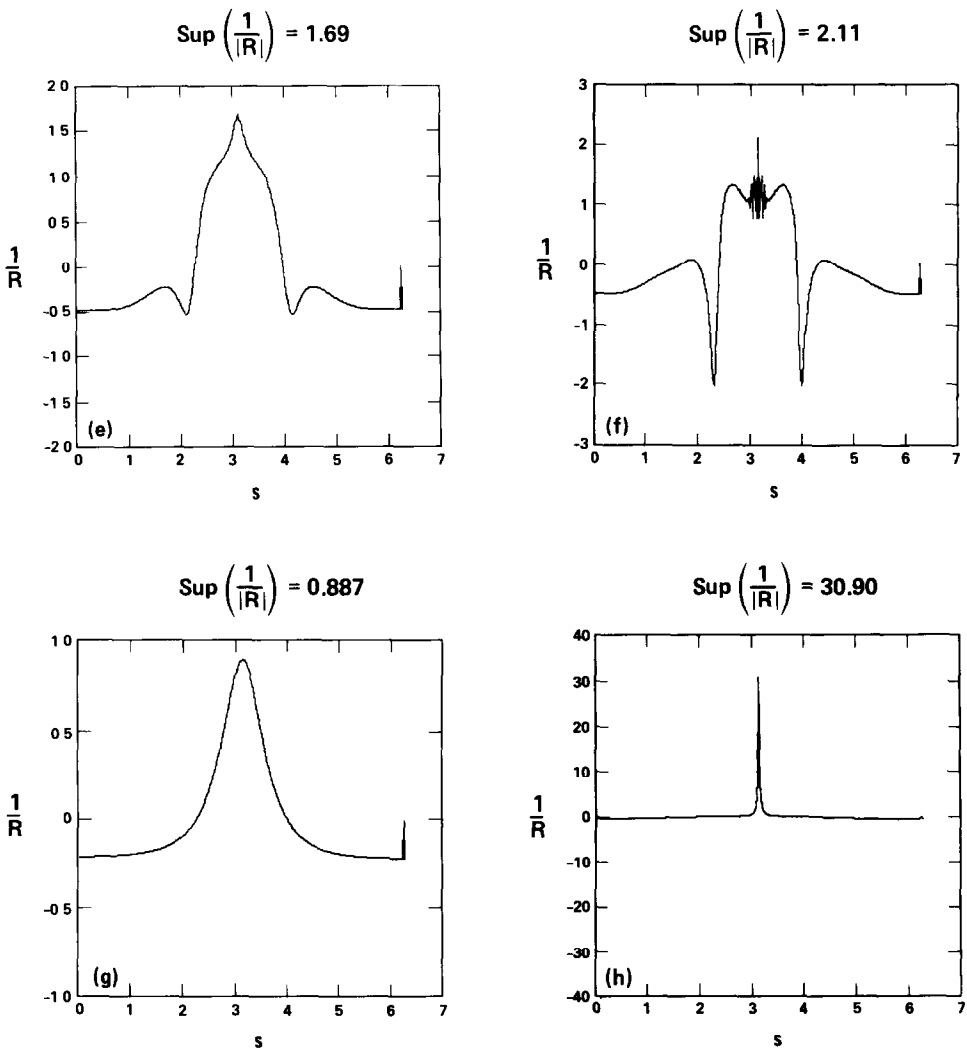

FIGURE 29—*Continued*

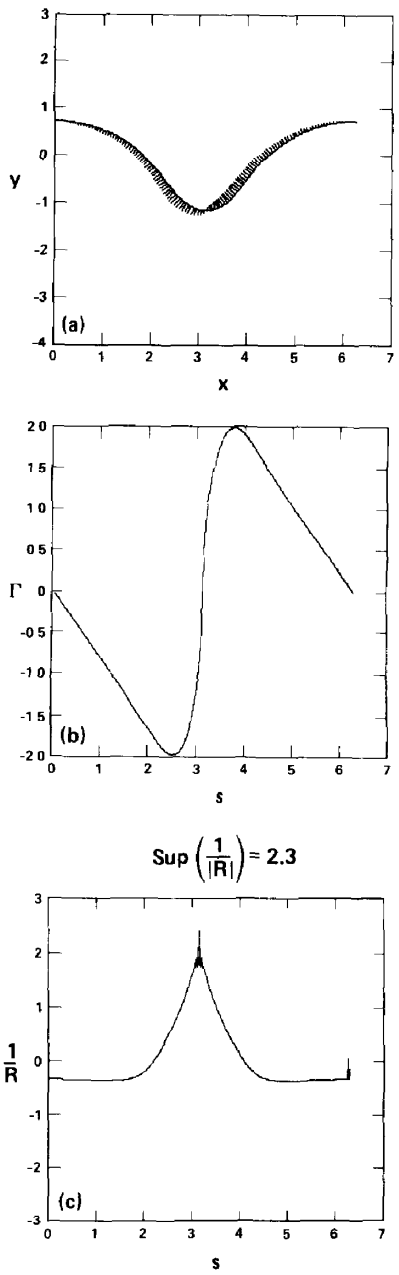

FIG 30. Interface, vortex-sheet strength Γ vs arclength and inverse curvature $1/R$ vs arclength for $A = 1$ and $\delta = 0.2$, 256 nodes used and $g = 1$ Node spreading used until $t = 3\,5$; restarted at $t = 3\,5$ with $\alpha = -0\,8$, (a–c) $t = 3.6$, (c) sup $|1/R| = 2\,5$.

It has already been mentioned how the exponential growth of this peak, shown in Fig. 11, limits how long a boundary-integral calculation will last. For $A = 0.8$ this single peak in the curvature dominates the early development and its effect is seen after the double-peaked behavior in the roll-up region begins to develop.

In order to understand the effect of smoothing at high Atwood numbers Figs. 30a–c show the interface, vortex-sheet profile, and curvature profile for one time from a simulation with $A = 1$ and $\delta = 0.2$. The calculation that goes to $t = 3.6$ used node spreading until $t = 3.5$, then allowed the nodes to move with $\alpha = -0.8$ $t = 3.6$ is the last time for which the vorticity and curvature did not show a strong even–odd instability. For $A = 1$, finite δ calculations end earlier than those with $\delta = 0$ because the sharp peak in the curvature in Fig. 30c at the tip of the spike is wider than the peak for $\delta = 0$ in Figs. 29g, h and it was difficult to find a means of distributing the nodes that provides adequate resolution over the entire interface.

VII. Conclusions

When this project was begun, it was hoped that the boundary-integral code of Baker, Meiron, and Orszag [10] could easily be extended to $A < 1$ by applying the smoothing of Krasny to eliminate the Kelvin–Helmholtz singularity. In the sense that no new singularities have been found and there are no indications that the problem remains ill-posed with this modification, this effort has succeeded. But numerous additional modifications of the numerical algorithms of the original code have been required in order to provide the resolution and accuracy needed to do interesting calculations. These modifications are necessary because resolving both the vorticity and curvature presents greater difficulties than in earlier Kelvin–Helmholtz boundary-integral calculations. Unlike using vortex blobs, they do not change the physics.

The general trend of these modifications has been to use algorithms that are lower order than those used by [10]. Although second-order algorithms have been used where possible to achieve convergence, in the early stages of developing this method, first-order algorithms often proved adequate. Lundgren [29] uses first-order algorithms and has had reasonable success. This is similiar to the trends in simulations of shocks where a bit of extra numerical diffusion often gives better simulations and there are elements of shock behavior in the vorticity profiles of our simulation. The lesson for problems with sharp discontinuities is that first order does work, but to get convergence some effort should be made to use second-order algorithms.

With these modifications, the boundary-integral method with vortex blobs has been able to identify several stages of development that occur for all Atwood numbers between 0 and 1. First, a spike develops, as it does for $A = 1$. Across the end of the spike is a sharp vorticity gradient, with two peaks of the vorticity on either side of the spike. Then some pinching at the end of the spike occurs, as if a droplet wants to form at the end of the spike as in the viscous Hele–Shaw instability. But

instead of this, the vorticity peaks on either side of the spike become dominated by the Kelvin–Helmholtz instability and the interface begins to roll up around these points. Instead of a droplet forming at the end of the spike, droplets form at the edge of the rollup regions and lead the rollups. For large Atwood numbers these later stages occur only after the spike is well developed. As the Atwood number or the blob size δ goes to zero, the rollup occurs earlier. For $A = 0.1$ and $\delta = 0.2$ the droplets became noticeable only during the late stages. For $A = 0$ droplets never form at the tips of the rollup.

These stages of development are consistent with previous calculations of the Rayleigh–Taylor instability and the objective of obtaining a calculation that can be used for inspiring and checking more powerful methods has been met. The next step should be a calculation that represents the effects of viscosity in a more realistic manner. For example a nonlinear prescription for the blob size as a function of arclength and time that is closer to the Navier–Stokes equations and reproduces the correct initial viscous growth [4–6] would be desirable. Questions concerning the use of time-varying blobs raised by Greengard [37] must be answered before this is attempted. Until such a method a available, it is pointless to further investigate questions such as whether there are asymptotic spike and bubble velocities, since preliminary evidence suggests that the type of smoothing does have a small effect upon these results.

Even if all these demands are met it would be very difficult to design experiments that looked at a single Rayleigh–Taylor mode and get comparisons. Although limited, some comparisons with multi-mode experiments, such as Read [38], could be done. For example, these simulations suggest that for smaller Atwood numbers and viscosities that the Kelvin–Helmholtz instability causes most of the breakup to occur along the edges of the spikes and this is observed in experiments. Our simulations suggest that only for large Atwood numbers coupled with large viscosities would droplet formation at the end of the spikes be expected. For true comparisons with these experiments multi-mode calculations must be done, but since the calculation cost goes as n^3, this will not be reasonable until the quadrature is improved, either by reducing the number of operations or new algorithms.

A vortex-in-cell method could provide an inexpensive alternative to quadrature and Tryggvason [39] uses two modifications of the vortex-in-cell method of [30] for $0 < A < 1$. Another possibility for reducing the cost while avoiding the smoothing inherent in vortex-in-cell methods would be to apply local corrections between nodes in neighboring cells of the vortex-in-cell grid as in Anderson [40]. The new scheme of Rohklin [41] might also provide a fast alternative. In all of these methods, the smoothing onto the mesh without local corrections should produce effects similiar to the finite δ calculations discussed here. For $A = 0$ this is demonstrated by Fig. 5. But in general, smoothing onto and interpolating from a mesh to the interface can introduce additional errors or smoothings that are not included in our simulations. The major qualitative difference between the vortex-in-cell calculations of [39] and the vortex-blob calculations discussed here for $A > 0$ is the amount of rollup. The accelerated-potential method (ACP) of [39] has more

rollup for $0 < A < 0.6$ than appears here and the iterated timestep method (ITS) appears to have less rollup. The source of this difference has been identified with the way the $\frac{1}{8}(\partial/\partial e)(\gamma^2/z_e z_e^*)$ term in (15a) is treated. We have crude empirical evidence that a vortex-in-cell code that corrects this term and uses spectral transforms and filtering as suggested by Buneman, Couët, and Leonard [42] will converge to the vortex-blob calculations discussed here. Tryggvason (private communication) has shown empirically that a vortex-blob method with additional smoothing of this term will give results that are qualitatively closer to the ACP results of [39]. Since the results appear to depend upon the smoothing used, better comparisons with true viscous calculations are needed, possibly using the method of Glimm *et al.* [12].

With the existing code several physical problems characterized by accelerating interfaces and unstably stratified fluids can be studied. The classic example is the implosion of inertial-fusion capsules, where there is a sharp density difference between the outer ablating shell and the fuel. Liquid fuel in tanks of space and aircraft also are subjected to strong accelerations. In the atmosphere the growth of cold surface layers as they are heated, expand, and then push into and mix with the overlying air is similar to the Taylor problem. Besides the physical applications, the Taylor problem is an example of a growing list of non-linear phenomena. It is closely related to Hele–Shaw flow and by analogy to problems in dendritic crystal growth. Singularities associated with two-dimensional Navier–Stokes flow are modified by the vorticity-production term in the Taylor problem, much as vorticity-production terms in two-dimensional magnetohydrodynamics and three-dimension turbulence change the nature of the singularities.

ACKNOWLEDGMENTS

I thank C Leith for initiating and supporting this project and I acknowledge useful discussions with R Chin and J Viecelli I thank T Lundgren, G Tryggvason, and E. Overman for communicating their results prior to publication.

REFERENCES

1 LORD RAYLEIGH, *Scientific Papers*, II, p. 200 (Cambridge, 1900)
2 G I. TAYLOR, *Proc Roy Soc London A* **201**, 192 (1950)
3 R BELLMAN AND R H PENNINGTON, *Q J. Appl Math* **12**, 151 (1954)
4 S CHANDRASEKAR, *Hydrodynamic and Hydromagnetic Stability* (Oxford Univ Press, London, 1961).
5 R MENIKOFF, R C MJOLSNESS, D H SHARP, AND C ZEMACH, *Phys Fluids* **20**, 2000 (1977)
6 R MENIKOFF, R C MJOLSNESS, D H SHARP, C ZEMACH, AND B J DOYLE, *Phys Fluids* **21**, 1674 (1978)
7 D H SHARP, *Phys D* **12**, 3 (1984)
8 R RICHTMYER, *Comm. Pure Appl Math* **13**, 297 (1960)
9 Y Y MESHKOF, *Izv. Akad. Nauk SSSR, Mekh Zhidk Gaza.* **151**, Sept–Oct. (1969)
10 G R BAKER, D I MEIRON, AND S A ORSZAG, *J Fluid Mech* **123**, 477 (1982).

11 B J DALY, *Phys Fluids* **10**, 297 (1967)
12 J. GLIMM, O MCBRYAN, R MENIKOFF, AND D H SHARP, *Siam J Sci Stat Comput* **7**, 230 (1986)
13. G R BAKER, D I MEIRON, AND S A ORSZAG, *Phys Fluids* **23**, 1485 (1980)
14 D I PULLIN, *J Fluid Mech* **119**, 507 (1982)
15 R C MENIKOFF AND C ZEMACH, *J Comput Phys.* **51**, 28 (1983)
16 G TRYGGVASON AND H AREF, *J. Fluid Mech* **136**, 1 (1983)
17 G. TRYGGVASON AND H AREF, *J. Fluid Mech* **154**, 284 (1985)
18 E A OVERMAN, II, N J ZABUSKY, AND S L OSSAKOW, *Phys. Fluids* **26**, 1139 (1983)
19 D W MOORE, *Proc Roy. Soc London A* **365**, 105 (1979)
20 D I MEIRON, G R BAKER, AND S A ORSZAG, *J Fluid Mech.* **114**, 283 (1982)
21 R KRASNY, *J Fluid Mech.* **167**, 65 (1986).
22 C M HO AND P HUERRE, *Ann Rev Fluid Mech* **16**, 365 (1984)
23 J J RILEY, R W METCALF, AND S A ORSZAG, *Phys Fluids* **29**, 406 (1986)
24. C POZRIKIDIS AND J J L HIGDON, *J Fluid Mech* **157**, 225 (1985)
25 E A OVERMAN, II AND N J ZABUSKY, *Phys Fluids* **25**, 1297 (1982)
26 R KRASNY, *J Comput Phys* **65**, 292 (1986).
27 J T BEALE AND A MAJDA, *J Comput Phys* **58**, 188 (1985)
28 C R ANDERSON, *J Comput Phys* **61**, 417 (1985)
29. T LUNDGREN, Regularization of vortex sheet computations, 1986 (unpublished)
30. H AREF AND G TRYGGVASON, Numerical experiments on the Rayleigh–Taylor instability for weakly stratified fluid with a sharp interface, 1986 (unpublished)
31 N J ZABUSKY AND E A OVERMAN, II, *J Comput Phys.* **52**, 351 (1983).
32 A ROBERT, *J Meteorol Soc Japan* **60**, 319 (1982)
33 R M KERR, Analysis of Rayleigh–Taylor flows using vortex blobs, UCID-20915, 1986 (unpublished)
34 B J DALY, *Phys Fluids* **12**, 1340 (1969)
35 R KRASNY, Computation of vortex sheet roll-up in the Trefftz plane, 1986 (preprint)
36 C GREENGARD, *J Comput Phys* **61**, 345 (1985)
37 M E BRACHET, M MENEGUZZI, AND P L SULEM, *Phys Rev Lett* **57**, 683 (1986)
38 K I READ, *Phys D* **12**, 45 (1984)
39 G TRYGGVASON, Numerical simulation of the Rayleigh–Taylor instability, *J Comput. Phys*, in press
40 C ANDERSON, *J Comput Phys* **62**, 111 (1986)
41 V ROHKLIN, *J. Comput. Phys.* **60**, 187 (1985)
42 O BUNEMAN, B COUET, AND A LEONARD, *J Comput Phys* **39**, 305 (1981)